Monthly Notices
of the
ROYAL ASTRONOMICAL SOCIETY

MNRAS **468,** 835–848 (2017)
Advance Access publication 2017 February 28

doi:10.1093/mnras/stx500

HATS-22b, HATS-23b and HATS-24b: three new transiting super-Jupiters from the HATSouth project

J. Bento,[1⋆] B. Schmidt,[1] J. D. Hartman,[2] G. Á. Bakos,[2] S. Ciceri,[3,4] R. Brahm,[5] D. Bayliss,[6] N. Espinoza,[5] G. Zhou,[7] M. Rabus,[3,5] W. Bhatti,[2] K. Penev,[2] Z. Csubry,[2] A. Jordán,[3,5] L. Mancini,[3] T. Henning,[3] M. de Val-Borro,[2] C. G. Tinney,[8,9] D. J. Wright,[8,9] S. Durkan,[10] V. Suc,[5] R. Noyes,[7] J. Lázár,[11] I. Papp[11] and P. Sári[11]

[1]*Research School of Astronomy and Astrophysics, Mount Stromlo Observatory, Australian National University, Cotter Road, Weston, ACT 2611, Australia*
[2]*Department of Astrophysical Sciences, Princeton University, 4 Ivy Ln., Princeton, NJ 08544, USA*
[3]*Max Plank Institute for Astronomy, Königstuhl 17, D-69117 Heidelberg, Germany*
[4]*Department of Astronomy, Stockholm University, SE-106 91 Stockholm, Sweden*
[5]*Instituto de Astrofísica, Facultad de Física, Pontificia Universidad Católica de Chile, Av. Vicuña Mackenna 4860, 7820436 Macul, Santiago, Chile*
[6]*Observatoire Astronomique de l'Université de Genéve, 51 ch. des Maillettes, CH-1290 Versoix, Switzerland*
[7]*Harvard-Smithsonian Center for Astrophysics, Cambridge, MA 02138, USA*
[8]*Australian Centre for Astrobiology, School of Physics, University of New South Wales, NSW 2052, Australia*
[9]*Exoplanetary Science at UNSW, School of Physics, University of New South Wales, NSW 2052, Australia*
[10]*Astrophysics Research Centre, School of Mathematics & Physics, Queen's University, Belfast BT7 1NN, UK*
[11]*Hungarian Astronomical Association, Budapest, 1461 Hungary*

Accepted 2017 February 24. Received 2017 February 19; in original form 2016 July 2

ABSTRACT

We report the discovery of three moderately high-mass transiting hot Jupiters from the HATSouth survey: HATS-22b, HATS-23b and HATS-24b. These planets add to the number of known planets in the $\sim 2 M_{\rm J}$ regime. HATS-22b is a $2.74 \pm 0.11\,M_{\rm J}$ mass and $0.953^{+0.048}_{-0.029}\,R_{\rm J}$ radius planet orbiting a $V = 13.455 \pm 0.040$ sub-solar mass ($M_* = 0.759 \pm 0.019\,{\rm M}_\odot$; $R_* = 0.759 \pm 0.019\,{\rm R}_\odot$) K-dwarf host star on an eccentric ($e = 0.079 \pm 0.026$) orbit. This planet's high planet-to-stellar mass ratio is further evidence that migration mechanisms for hot Jupiters may rely on exciting orbital eccentricities that bring the planets closer to their parent stars followed by tidal circularization. HATS-23b is a $1.478 \pm 0.080\,M_{\rm J}$ mass and $1.69 \pm 0.24\,R_{\rm J}$ radius planet on a grazing orbit around a $V = 13.901 \pm 0.010$ G-dwarf with properties very similar to those of the Sun ($M_* = 1.115 \pm 0.054$; $R_* = 1.145 \pm 0.070$). HATS-24b orbits a moderately bright $V = 12.830 \pm 0.010$ F-dwarf star ($M_* = 1.218 \pm 0.036\,{\rm M}_\odot$; $R_\star = 1.194^{+0.066}_{-0.041}\,{\rm R}_\odot$). This planet has a mass of $2.39^{+0.21}_{-0.12}\,M_{\rm J}$ and an inflated radius of $1.516^{+0.085}_{-0.065}\,R_{\rm J}$.

Key words: techniques: photometric – techniques: spectroscopic – stars: individual: HATS-22 – stars: individual: GSC 6664-00373 – stars: individual: HATS-23 – stars: individual: GSC 8382-01464 – stars: individual: HATS-24 – stars: individual: GSC 9054-00129 – planetary systems.

1 INTRODUCTION

Transiting planets are the key towards understanding the structure and composition of planetary systems. The breadth of system parameters that can be determined from the discovery data sets and follow-up studies surpasses any other detection method, the most important being the mass and radius, yielding an estimate of the bulk density. Moreover, these planets are amenable to transmission studies during transit (e.g. Seager & Sasselov 2000; Pont et al. 2008; Sing et al. 2011; Jordán et al. 2013; Marley et al. 2013; Bento et al. 2014), a direct measurement of the planet's day-side emission as an estimate of the surface temperature during secondary eclipse (Knutson et al. 2008; Croll et al. 2011; Désert et al. 2011; Zhou et al. 2013, 2014), and other properties (Collier Cameron et al. 2010; Gandolfi et al. 2012; Hartman et al. 2015; Louden & Wheatley 2015; Zhou et al. 2016).

In particular, the hundreds of hot Jupiters (broadly Jupiter mass planets orbiting close to their host stars on less than ∼10 d periods) found to date have challenged planetary formation theories

⋆ E-mail: joao.bento@anu.edu.au

and structure models. Despite an early suggestion of the possibility that such planets may exist by Struve (1952), explaining their existence is not trivial as they are not generally expected to form *in situ* (Boss 1995; Lissauer 1995; Bodenheimer, Hubickyj & Lissauer 2000), with the migration potentially taking place in the very early stages of formation (Donati et al. 2016). Recent work suggests that there is a potential mechanism that can form such planets *in situ* (Batygin, Bodenheimer & Laughlin 2016), but the general consensus is that these planets are formed at large separations and migrate inwards to their current positions, and several possible mechanisms have been suggested for this process. A disc migration scenario has been proposed in which the orbiting planet exchanges angular momentum with the protoplanetary disc and loses orbital momentum, thereby starting out at large separations and making its way in to close to the host star (e.g. Alibert et al. 2005; Chambers 2009; Rice, Armitage & Hogg 2008, and references therein). Alternatively, interactions with other bodies in the system can cause scattering/ejection events and the planet in question is forced into an eccentric orbit that brings it closer to the host star (e.g. Rasio & Ford 1996; Ford & Rasio 2008). Tidal interactions are then thought to circularize the orbit resulting in close-in planets. Other processes suggested include Kozai migration, first proposed by Wu & Murray (2003), which states that a highly inclined stellar companion can induce Kozai oscillations (Kozai 1962) in the planet and excite it to progressively higher eccentricity. We note, however, that Ngo et al. (2016) suggest that only a small fraction (<20 per cent) of hot Jupiter host stars have stellar companions capable of inducing such oscillations. Very recent works by Petrovich (2015) and Wu & > Lithwick (2011) suggest that *secular migrations* may occur due to interactions between two or more well-spaced, eccentric planets, which can cause one of them to become very eccentric on long time-scales, leading to both enhanced eccentricity and tidal dissipation over larger time-scales (Lithwick & Wu 2011). However, recent results show that an understanding of planet formation and migration has not been achieved yet. Antonini, Hamers & Lithwick (2016) suggest that perhaps hot Jupiters with outer companions are unlikely to have migrated through high-eccentricity processes due to the instability of their orbits, while Schlaufman & Winn (2016) find that warm Jupiters are no more likely to have wide-orbit planetary companions than those in longer orbits, which is at odds with an eccentric migration scenario.

The possibility that there is a mass dependence in the question of planet migration and eccentricity is supported by evidence that higher mass planets tend to show higher eccentricity than those less massive than $2M_J$ (Mazeh, Mayor & Latham 1997; Marcy et al. 2005; Southworth et al. 2009). Moreover, it seems that planets at higher orbital separation/period also have a higher tendency to show non-zero eccentricities (Pont et al. 2011) versus close-in planets. This raises questions such as: are high-mass planets more susceptible to retain large eccentricities on longer time-scales? And, if so, is this an indication that planet–planet scattering, predicted to generate high eccentric orbits, is likely to be the main migration mechanism for planetary systems? Is the structure and evolution of high- and low-mass planets fundamentally different? Are hot Jupiter structures fundamentally affected by extreme cases of inward migration and current irradiation levels? The answer lies in a larger sample and better understanding of the composition of these planets.

In this paper, we report the discovery of three new transiting super-Jupiters with masses higher than $1.4M_J$ from the HATSouth survey: HATS-22b, HATS-23b and HATS-24b. These planets add to the list of well-characterized massive hot Jupiters that collectively pose a challenge to models of planetary formation and migration.

In Section 2, we describe the photometric and spectroscopic observations undertaken for all three targets in the pursuit of determining their planetary nature. Section 3 contains a description of the global data analysis and presents the modelled stellar and planetary parameters. We also describe the methods employed to reject false positive scenarios. Our findings are finally discussed in Section 4.

2 OBSERVATIONS

Periodic planetary transit-like signals in any time series photometric survey can be created by a range of astrophysical events that include grazing binary stellar eclipses, transits by planet-sized dwarf stars and eclipsing binary systems whose light is blended with a nearby foreground or background star. As such, a substantial follow-up campaign is required using both photometric and spectroscopic observations. In this section, we describe the full set of observations that led to the detection and confirmation of the planets presented in this paper.

2.1 Photometric detection

The HATSouth project is a collaboration between Princeton, the Australian National University (ANU), the Max Plank Institute for Astronomy and the Pontificia Universidad Católica de Chile, dedicated to finding transiting planets hosted by bright stars in the Southern hemisphere (Bakos et al. 2013). It is the largest ground-based search for transiting extrasolar planets in the world, with a three-site network [Las Campanas Observatory in Chile, the High Energy Spectroscopic Survey (H.E.S.S.) site in Namibia and Siding Spring Observatory (SSO), Australia] capable of continuously monitoring 128 square degree fields in the Southern hemisphere. The project has commissioned six enclosures, two per site, each containing four telescopes on a single mount. Discoveries include the notable case of HATS-17b (Brahm et al. 2016), which is the largest period transiting exoplanet found to date from a ground-based survey, thereby demonstrating HATSouth's unique strength in its longitude coverage. A full list of discovered planets along with discovery light curves can be found at http://hatsouth.org/.

Table 1 shows a summary of the photometric observations for the planetary systems HATS-22, HATS-23 and HATS-24. For HATSouth data, we list the HATSouth unit, CCD and field name from which the observations were taken. The detection of all targets relied on data from all HATSouth telescopes, HS-1 and HS-2 located in Chile, HS-3 and HS-4 in Namibia and HS-5 and HS-6 in Australia. The data gathered at different time periods between 2011/04 and 2013/11 for different targets, as described in Table 1, resulted in a total of 13 129 data points for HATS-22, 22 937 observations of HATS-23 and 4406 points for HATS-24.

All HATSouth observations are obtained through a Sloan *r* filter with a typical exposure time of 240 s. The data were reduced with the custom pipeline described by Penev et al. (2013) and the light curves were detrended using an External Parameter Decorrelation (EPD) method (Bakos et al. 2013) followed by the application of the Trend-Filtering Algorithm (TFA; Kovács, Bakos & Noyes 2005). A Box Least-Squares (BLS) algorithm (see Kovács, Zucker & Mazeh 2002) was then used to search for periodic transit-like signals. The resulting discovery light curves phase-folded to the highest likelihood periods are shown in Fig. 1.

After having removed the best-fitting BLS model corresponding to the hot Jupiter transit signal from the light curves, we searched

Table 1. Summary of photometric observations.

Instrument/field[a]	Date(s)	No. of images	Cadence[b] (s)	Filter	Precision[c] (mmag)
HATS-22					
HS-2.2/G610	2011 Apr–2013 July	5368	280	*r*	7.9
HS-4.2/G610	2013 Jan–2013 July	3755	289	*r*	7.2
HS-6.2/G610	2011 Apr–2013 July	4006	282	*r*	7.6
LCOGT 1 m+CTIO/sinistro	2015 Mar 30	85	226	*i*	1.0
HATS-23					
HS-1.2/G747	2013 Mar–2013 Oct	4233	287	*r*	12.6
HS-2.2/G747	2013 Sept–2013 Oct	648	287	*r*	12.3
HS-3.2/G747	2013 Apr–2013 Nov	9020	297	*r*	12.1
HS-4.2/G747	2013 Sept–2013 Nov	1460	297	*r*	13.6
HS-5.2/G747	2013 Mar–2013 Nov	6013	297	*r*	11.9
HS-6.2/G747	2013 Sept–2013 Nov	1563	290	*r*	14.9
LCOGT 1 m+SSO/SBIG	2015 July 07	22	194	*i*	2.1
Swope 1 m/e2v[d]	2015 July 15	51	139	*i*	13.7
LCOGT 1 m+SSO/SBIG	2015 Aug 30	34	192	*i*	3.1
LCOGT 1 m+CTIO/sinistro	2015 Sept 05	47	223	*i*	1.2
LCOGT 1 m+SAAO/SBIG	2015 Sept 16	39	201	*z*	4.8
HATS-24					
HS-1.1/G777	2011 May–2012 Sept	1513	298	*r*	9.1
HS-3.1/G777	2011 July–2012 Sept	1688	297	*r*	9.4
HS-5.1/G777	2011 May–2012 Sept	1205	296	*r*	9.3
LCOGT 1 m+SAAO/SBIG	2015 June 07	90	151	*i*	1.6

Notes. [a]For HATSouth data, we list the HATSouth unit, CCD and field name from which the observations are taken. HS-1 and HS-2 are located at Las Campanas Observatory in Chile, HS-3 and HS-4 are located at the H.E.S.S. site in Namibia, and HS-5 and HS-6 are located at SSO in Australia. Each unit has four CCDs. Each field corresponds to one of 838 fixed pointings used to cover the full 4π celestial sphere. All data from a given HATSouth field and CCD number are reduced together, while detrending through external parameter decorrelation (EPD) is done independently for each unique unit+CCD+field combination.
[b]The median time between consecutive images rounded to the nearest second. Due to factors such as weather, the day–night cycle, guiding and focus corrections, the cadence is only approximately uniform over short time-scales.
[c]The rms of the residuals from the best-fitting model.
[d]The Swope 1 m observations of HATS-23 produced very poor quality photometry due to adverse weather conditions, so we excluded them from the analysis of this system.

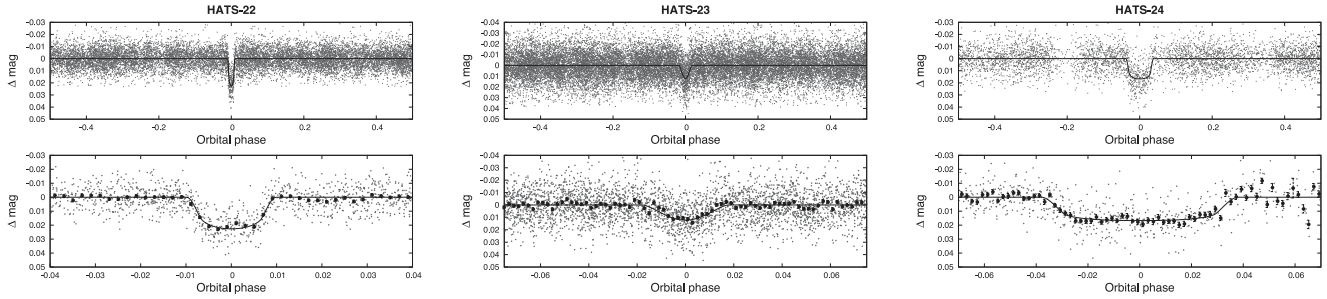

Figure 1. Phase-folded unbinned HATSouth light curves for HATS-22 (left), HATS-23 (middle) and HATS-24 (right). In each case, we show two panels. The top panel shows the full light curve, while the bottom panel shows the light curve zoomed-in on the transit. The solid lines show the model fits to the light curves. The dark filled circles in the bottom panels show the light curves binned in phase with a bin size of 0.002.

for additional periodic signals with the aim to detect potential stellar activity or other transiting planets in each of the three systems. The light curves for all targets did not reveal any other significant signals, defined as those with a formal false alarm probability, assuming Gaussian white noise, of less than 0.1 per cent, on a second BLS pass of the residuals. We therefore find no evidence for additional transiting planets in the systems. However, a generalized Lomb–Scargle (Zechmeister & Kürster 2009) routine, looking for sinusoidal patterns that can be related to activity, revealed a significant peak at a period of 7.49 ± 0.25 d for HATS-23 with a false alarm probability of 10^{-21}. This is shown in Fig. 2 (left-hand panel). Further inspection of this signal reveals a sinusoidal signal (right-hand panel) that can be attributed to activity such as stellar spots on the surface of the host star modulating the light curve. We note that the detected 7.49 d period is not consistent with the stellar rotation period estimated from $v \sin i$ (13.1 ± 1.4 d) assuming an aligned stellar rotation axis. If the detected sinusoidal signal is indeed real and related to the stellar rotation, this may suggest a moderately high misalignment between the orbital plane and the stellar rotational axis. On the other hand, we cannot definitively exclude the

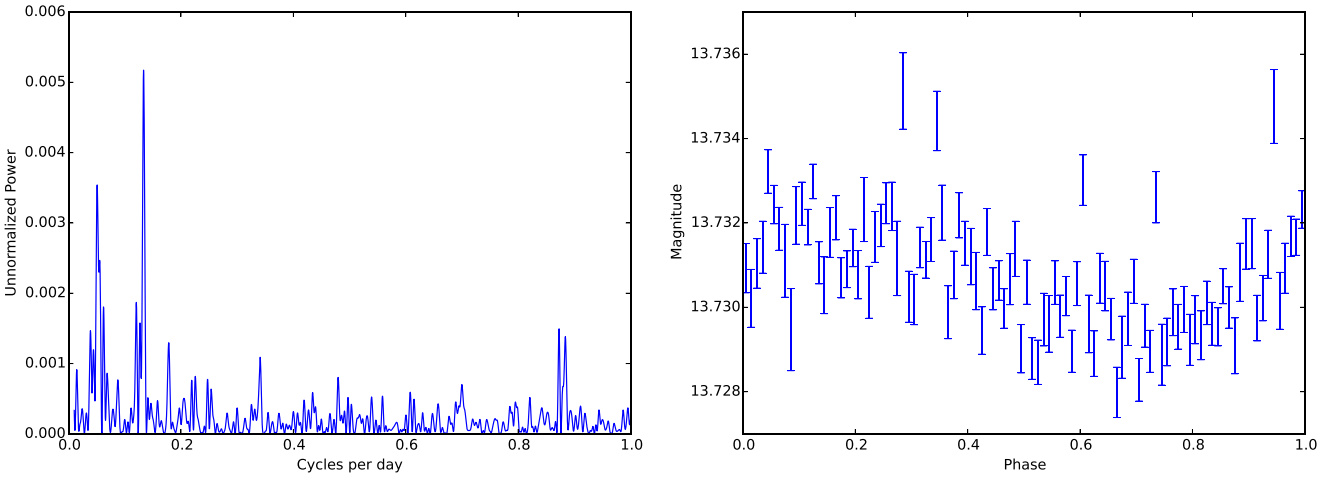

Figure 2. Additional period detected on the discovery light curve of HATS-23b. Left: we show the Lomb–Scargle periodogram produced using the method of Zechmeister & Kürster (2009) after removal of the transit signal. Right: the phase-folded light curve on the 7.4965 d period equivalent to the highest peak binned in 0.01 phase intervals. The error bars shown are calculated through post-binning error propagation of the original magnitude errors of individual measurements.

possibility that the true rotation period is double this value, which would be consistent with the observed $v \sin i$. However, when the light curve is folded at twice the 7.49 d period, it reveals a double oscillation and the power of the window function at this period is substantially lower. Nevertheless, more observations of this system are required to address this dichotomy.

2.2 Spectroscopic observations

2.2.1 Reconnaissance spectroscopic observations

The initial follow-up phase for all HATSouth planet candidates is carried out with reconnaissance spectra taken with the WiFeS instrument on the 2.3 m ANU telescope at SSO (Dopita et al. 2007). Observations at $R \equiv \Delta\lambda/\lambda \approx 3000$ were taken to determine the stellar type of the host star, using the blue arm of the spectrograph. We estimate three key stellar properties, the effective temperature $T_{\rm eff}$, $\log g_*$ and [Fe/H], by performing a grid search minimizing the χ^2 between the observed normalized spectrum and synthetic templates from the MARCS model atmospheres (Gustafsson et al. 2008). 2MASS $J - K$ colours are used to restrict the $T_{\rm eff}$ parameter space and extinction correction is applied using the method of Cardelli, Clayton & Mathis (1989). A detailed description of the observing and data reduction procedure is described in Bayliss et al. (2013). This type of observation is performed to identify giant host stars, for which the observed dip in its light curve could only have been caused by a stellar companion, and to identify stars not suitable for precise radial velocity (RV) follow-up due to high $T_{\rm eff}$ or high $v \sin i$. In addition, observations are taken at predicted quadrature phase with WiFeS using a mid-resolution $R \sim 7000$ grating to perform RV measurements at a precision of $\sim$2 km s^{-1}. We use a cross-correlation method against RV standards observed every night, using bracketed Ne–Ar exposures and a selection of telluric lines for calibration. This is, however, dependent on stellar type and signal-to-noise of each individual target. This allows for the detection of RV variations above $\sim$5 km s^{-1}, and the exclusion of any targets showing large variations indicating that the transiting companion is a star. Details of these observations can be found in Table 2 and are described here.

(i) For HATS-22, we found an effective temperature of 4600 ± 300 K, $\log g_*$ of 4.8 ± 0.3 dex and metallicity of [Fe/H] $= -0.5 \pm 0.5$ dex, leading to the conclusion that this is a K-dwarf host star. Two measurements showed no clear variation at quadrature.

(ii) For HATS-23, we found an effective temperature estimate of 5900 ± 300 K, $\log g_*$ of 4.5 ± 0.3 dex and metallicity of [Fe/H] $= 0.0 \pm 0.5$ dex. We conclude that the host star is of F- or G-type. A single RV measurement with WiFeS was taken but later complemented by observations with the FEROS spectrograph (see Section 2.2.2).

(iii) HATS-24 was found to have an effective temperature of 5800 ± 300 K, $\log g_*$ of 3.4 ± 0.3 dex and metallicity of [Fe/H] $= -0.5 \pm 0.5$ dex. Based on this, we concluded that the target is a G or F star, but the surface gravity suggested that this is a sub-giant. Three RV measurements taken showed no significant variation in the covered orbital phase.

Having excluded clear eclipsing binaries and giant host stars, these targets were then promoted to the next steps in the follow-up campaign, leading to further higher RV precision spectroscopy and photometric follow-up.

2.2.2 High-precision spectroscopic observations

A full RV characterization covering a wide portion of the orbital phase of all of our targets is required in order to determine fundamental parameters such as mass and eccentricity of the orbits. Observations with the High Accuracy Radial Velocity Planet Searcher (HARPS; Mayor et al. 2003), fed by the European Southern Observatory (ESO) 3.6 m telescope at $R \sim 115\,000$, were obtained for HATS-22 and HATS-24, as well as $R \sim 60\,000$ spectra using the CORALIE spectrograph (Queloz et al. 2001) fed by the 1.2 m Euler telescope, both located at La Silla Observatory (LSO), Chile. All three targets were also monitored for RV measurements using the FEROS spectrograph (Kaufer & Pasquini 1998, $R \sim 48\,000$) fed by the MPG 2.2 m telescope at LSO. The data reduction for all these spectra was performed using the method described in Jordán et al. (2014), with modifications to accommodate the different formats of the FEROS and HARPS data. Additionally, 11 spectra of HATS-24 were also obtained at $R \sim 70\,000$ with the CYCLOPS2 fibre-fed

Table 2. Summary of spectroscopy observations.

Instrument	UT date(s)	# Spec.	Res. $\Delta\lambda/\lambda/1000$	S/N range[a]	γ_{RV}[b] (km s^{-1})	RV precision[c] (m s^{-1})
HATS-22						
ESO 3.6 m/HARPS	2015 Feb–Apr	4	115	8–18	−7.370	15
Euler 1.2 m/CORALIE	2015 Feb–June	7	60	10–14	−7.414	35
ANU 2.3 m/WiFeS	2015 Feb 28	1	3	44	–	–
ANU 2.3 m/WiFeS	2015 Feb–Mar	2	7	63–83	−7.7	4000
MPG 2.2 m/FEROS	2015 Apr–June	4	48	43–58	−7.438	25
HATS-23						
ANU 2.3 m/WiFeS	2015 June 1	1	3	43	–	–
ANU 2.3 m/WiFeS	2015 June 1	1	7	39	−13.8	4000
MPG 2.2 m/FEROS	2015 June 8–18	8	48	18–39	−13.372	16
HATS-24						
ANU 2.3 m/WiFeS	2015 Feb 1	1	3	29	–	–
ANU 2.3 m/WiFeS	2015 Feb 1–5	3	7	31–55	−7.1	4000
ESO 3.6 m/HARPS	2015 Apr 6–7	2	115	9–15	−3.370	120
AAT 3.9 m/CYCLOPS2+UCLES[d]	2015 May 6–13	11	70	10–27	−3.284	160
Euler 1.2 m/CORALIE	2015 June 6–8	3	60	14–17	−3.236	140
MPG 2.2 m/FEROS	2015 June 17–21	4	48	42–60	−3.259	43

Notes. [a]S/N per resolution element near 5180 Å.
[b]For high-precision RV observations included in the orbit determination, this is the zero-point RV from the best-fitting orbit. For other instruments, it is the mean value. We do not provide this quantity for the lower resolution WiFeS observations that were only used to measure stellar atmospheric parameters.
[c]For high-precision RV observations included in the orbit determination, this is the scatter in the RV residuals from the best-fitting orbit (which may include astrophysical jitter); for other instruments, this is either an estimate of the precision (not including jitter) or the measured standard deviation. We do not provide this quantity for low-resolution observations from the ANU 2.3 m/WiFeS.
[d]We excluded from the analysis two of the AAT 3.9 m/CYCLOPS2+UCLES observations of HATS-24 that were taken during transit.

and the UCLES spectrograph on the 3.9 m Anglo-Australian Telescope (AAT) at SSO and the data were reduced using the methods described in Addison et al. (2013). Further details about these observations can be found in Table 2. The resulting data sets for all targets can be found in Table 3 at the end of the paper, and are shown in Fig. 3, which includes RV curves, best-fitting models and bisector span (BS) estimates shown in the bottom panels for each target. All systems clearly show an RV variation consistent with the detected orbital period from the photometric light curves and no clear correlation between the RV measurements and the BSs, indicating that the systems are likely bona fide transiting planets (see Section 3.2).

2.3 Photometric follow-up observations

The three candidates were all photometrically followed up employing the Las Cumbres Observatory Global network of Telescopes (Brown et al. 2013), specifically using the 1-m-sized telescopes of this network. These observations are undertaken to confirm the transit signal as well as refine the derived transit parameters from the HATSouth photometry. A single full transit of HATS-22 was observed in 2015 March using the *i*-band filter in which 85 images at a 226 s cadence were obtained. A single transit of HATS-24 in June of the same year was also obtained, consisting of 90 images with 151 s cadence. Due to the grazing nature of HATS-23, a larger number of photometric follow-up observations were required. Two full and two partial transits of HATS-23 were observed between 2015 July and September (inclusive), the first three in the *i*-band and the last using the *z*-band filter. The light curves for these high-precision photometric observations are shown in Fig. 4 along with the best-fitting models. The photometric data were taken and reduced using the same strategy and methods described in Penev et al. (2013), with details of set-up in Bayliss et al. (2015), using a customizable pipeline. This pipeline uses standard photometric reduction frames (master bias, darks, twilight flats) and the DAOPHOT aperture photometry package for flux extraction of target and comparison stars. A quadratic trend in time as well as variations correlated with point spread function (PSF) shape were fitted simultaneously with the transit shape to compensate for differential refraction effects due to airmass and poor seeing. The 'V'-shaped transit signal for HATS-23 is clearly indicative of the grazing nature of the planetary system and the consistent depth of the transits in both observed bands for this target also suggests that this is not an eclipsing binary system or a hierarchical triple system. The data from all photometric follow-up are available in electronic format in Table 4 and all photometric follow-up observations are also summarized in Table 1.

2.4 Lucky imaging observations

High spatial resolution 'lucky' imaging observations were made of HATS-22 using the Astralux camera (Hippler et al. 2009) on the New Technology Telescope (NTT) at LSO on 2015/12/23. These observations are part of a campaign to detect potential companions for exoplanet host star candidates and place upper limits on magnitude contrasts. The data were taken using the Sloan Digital Sky Survey z' filter, resulting in a set of 10^4 images with an exposure time of 100 ms each. We used the Drizzle algorithm from Fruchter & Hook (2002) to combine a set of the best 10 per cent of images acquired and the result of these can be found in Fig. 5, where we show the 1 and 4 arcsec radii lines for reference. A slightly asymmetric extended profile is visible on this image likely due to instrumental effects, confirmed by taking images of other targets on

Table 3. Relative RVs and BSs for HATS-22 and HATS-23.

BJD (2450000+)	RV[a] ($m\,s^{-1}$)	σ_{RV}[b] ($m\,s^{-1}$)	BS ($m\,s^{-1}$)	σ_{BS} ($m\,s^{-1}$)	Phase	Instrument
			HATS-22			
7072.74688	432.36	8.00	−25.0	42.0	0.765	HARPS
7075.81290	−237.86	17.00	−113.0	32.0	0.414	CORALIE
7077.72945	381.14	18.00	18.0	32.0	0.820	CORALIE
7078.70639	−23.86	17.00	−10.0	32.0	0.027	CORALIE
7109.73325	170.14	22.00	125.0	43.0	0.596	CORALIE
7118.66166	−41.64	17.00	−9.0	74.0	0.487	HARPS
7119.60792	336.19	10.00	−33.0	13.0	0.687	FEROS
7119.67550	341.36	24.00	33.0	90.0	0.701	HARPS
7120.62753	326.36	16.00	−31.0	74.0	0.903	HARPS
7179.52938	−274.86	21.00	0.0	43.0	0.375	CORALIE
7180.51051	156.14	22.00	38.0	43.0	0.583	CORALIE
7181.51430	449.14	22.00	−141.0	43.0	0.795	CORALIE
7187.55141	−235.81	11.00	−51.0	15.0	0.073	FEROS
7187.57284	−206.81	11.00	21.0	15.0	0.078	FEROS
7187.59426	−276.81	12.00	−53.0	16.0	0.082	FEROS
			HATS-23			
7181.62180	−182.31	18.00	77.0	22.0	0.344	FEROS
7182.71745	175.69	19.00	72.0	23.0	0.851	FEROS
7183.66969	–	–	68.0	32.0	0.292	FEROS
7184.75104	–	–	7.0	32.0	0.793	FEROS
7185.72406	−226.31	16.00	77.0	19.0	0.243	FEROS
7186.85044	207.69	19.00	73.0	23.0	0.764	FEROS
7187.85244	−188.31	16.00	24.0	19.0	0.228	FEROS
7189.63018	−47.31	14.00	−17.0	17.0	0.051	FEROS
7190.81426	139.69	17.00	10.0	21.0	0.599	FEROS
7191.68515	−20.31	16.00	55.0	19.0	0.002	FEROS
			HATS-24			
7118.75825	−76.82	69.00	14.0	106.0	0.537	HARPS
7119.77652	−338.82	38.00	−132.0	56.0	0.292	HARPS
7149.08745[c]	−379.95	40.30	–	–	0.028	CYCLOPS
7149.10350[c]	−384.45	27.60	–	–	0.040	CYCLOPS
7149.11954	−44.25	61.00	–	–	0.052	CYCLOPS
7150.09608	393.15	56.20	–	–	0.776	CYCLOPS
7150.11204	242.95	55.80	–	–	0.788	CYCLOPS
7150.12799	395.45	41.60	–	–	0.799	CYCLOPS
7152.06340	−481.85	33.80	–	–	0.235	CYCLOPS
7152.07872	−509.25	21.00	–	–	0.246	CYCLOPS
7152.09403	−508.95	17.90	–	–	0.257	CYCLOPS
7156.13898	−798.25	96.80	–	–	0.257	CYCLOPS
7156.15505	−462.95	48.40	–	–	0.269	CYCLOPS
7179.70211	393.16	71.00	−20.0	43.0	0.731	CORALIE
7180.63482	−13.84	62.00	–	–	0.422	CORALIE
7181.69032	−465.84	57.00	−45.0	35.0	0.205	CORALIE
7190.68048	258.75	25.00	28.0	13.0	0.872	FEROS
7191.75911	383.75	31.00	81.0	16.0	0.672	FEROS
7193.86712	−370.25	28.00	56.0	14.0	0.235	FEROS
7194.55840	326.75	24.00	34.0	13.0	0.748	FEROS

Notes. [a]The zero-point of these velocities is arbitrary. An overall offset γ_{rel} fitted independently to the velocities from each instrument has been subtracted.

[b]Internal errors excluding the component of astrophysical jitter considered in Section 3.3.

[c]These observations were excluded from the analysis because the observations were (partially) obtained with the planet in transit, and thus may be affected by the Rossiter–McLaughlin effect.

different nights that show a similar feature. As such, while we can confirm that there is no clear bright star in the vicinity of our target, we cannot completely exclude the possibility that a faint close companion within 1 arcsec is not present. This is a generic problem with most confirmed transiting planets, and as such we further address this issue in Section 3.2 where we perform a blend analysis that increases our confidence that this is indeed a planetary body companion.

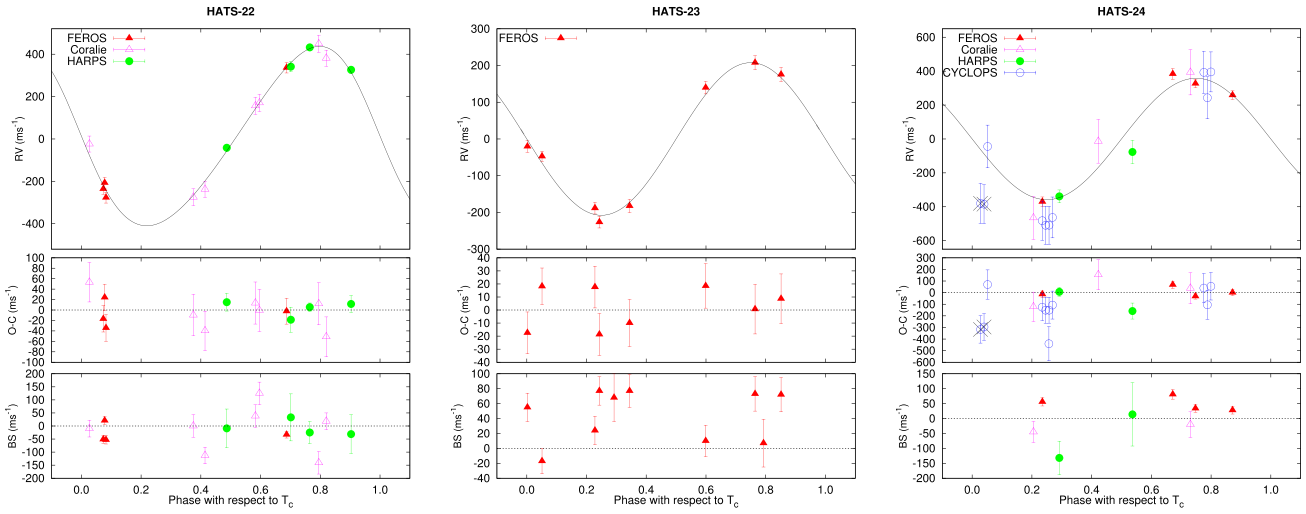

Figure 3. Phased high-precision RV measurements for HATS-22 (left), HATS-23 (middle) and HATS-24 (right). The instruments used are labelled in the plots. For HATS-24, two observations marked with an X were obtained (partially) in transit and have been excluded from the analysis. In each case, we display three panels. The top panel shows the phased measurements together with our best-fitting model (see Table 3) for each system where we show the RV jitter values for each case. Zero-phase corresponds to the time of mid-transit. The centre-of-mass velocity has been subtracted. The second panel displays the velocity O−C residuals from the best fit. The error bars include the jitter terms listed in Table 3 added in quadrature to the formal errors for each instrument. The third panel shows the bisector spans (BS). Note the different vertical scales of the panels.

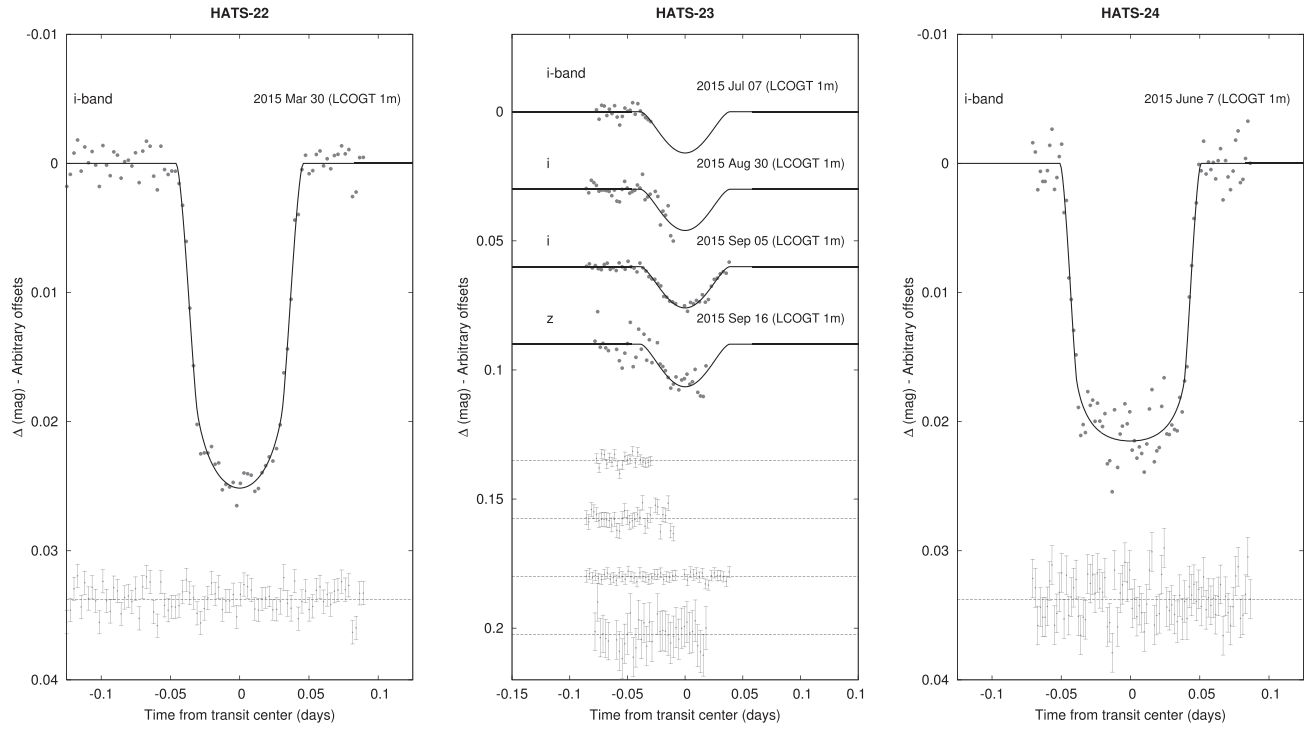

Figure 4. Unbinned transit light curves for HATS-22 (left), HATS-23 (middle) and HATS-24 (right). The light curves have been corrected for quadratic trends in time, and linear trends with up to three parameters characterizing the shape of the PSF, fitted simultaneously with the transit model. The dates of the events, filters and instruments used are indicated. Light curves following the first are displaced vertically for clarity. Our best fit from the global modelling described in Section 3.3 is shown by the solid lines. The residuals from the best-fitting model are shown below in the same order as the original light curves. The error bars represent the photon and background shot noise, plus the readout noise.

3 ANALYSIS

3.1 Properties of the parent star

We used the Zonal Atmospheric Stellar Parameter Estimator (ZASPE; Brahm et al. 2017) to model the stellar parameters of the host stars for all targets. ZASPE is capable of precise stellar atmospheric parameter estimation from high-resolution echelle spectra from FGK-type stars. It compares the observed spectrum with a grid of synthetic spectra by a least-squares minimization of the normalized continuum in only the most sensitive regions of the stellar spectrum.

Table 4. Light-curve data for HATS-22, HATS-23 and HATS-24.

Object[a]	BJD[b] (2400000+)	Mag[c]	$\sigma_{\rm Mag}$	Mag(orig)[d]	Filter	Instrument
HATS-22	56443.36356	−0.006 27	0.004 63	–	*r*	HS
HATS-22	56363.07603	0.005 98	0.004 73	–	*r*	HS
HATS-22	56466.97802	−0.004 07	0.005 61	–	*r*	HS
HATS-22	56396.13657	0.007 30	0.005 02	–	*r*	HS
HATS-22	56438.64228	−0.009 29	0.005 45	–	*r*	HS
HATS-22	56424.47483	−0.000 12	0.004 67	–	*r*	HS
HATS-22	56315.85060	−0.019 03	0.004 29	–	*r*	HS
HATS-22	56443.36694	0.011 29	0.004 68	–	*r*	HS
HATS-22	56424.47573	0.019 45	0.004 59	–	*r*	HS
HATS-22	56386.69363	0.011 08	0.004 55	–	*r*	HS

Notes. – This table is available in a machine-readable form in the online journal. A portion is shown here for guidance regarding its form and content.

[a]Either HATS-22, HATS-23 or HATS-24.

[b]Barycentric Julian Date is computed directly from the UTC time without correction for leap seconds.

[c]The out-of-transit level has been subtracted. For observations made with the HATSouth instruments (identified by 'HS' in the 'Instrument' column), these magnitudes have been corrected for trends using the EPD and TFA procedures applied *prior* to fitting the transit model. This procedure may lead to an artificial dilution in the transit depths. The blend factors for the HATSouth light curves are listed in Table 5. For observations made with follow-up instruments (anything other than 'HS' in the 'Instrument' column), the magnitudes have been corrected for a quadratic trend in time, and for variations correlated with up to three PSF shape parameters, fitted simultaneously with the transit.

[d]Raw magnitude values without correction for the quadratic trend in time, or for trends correlated with the seeing. These are only reported for the follow-up observations.

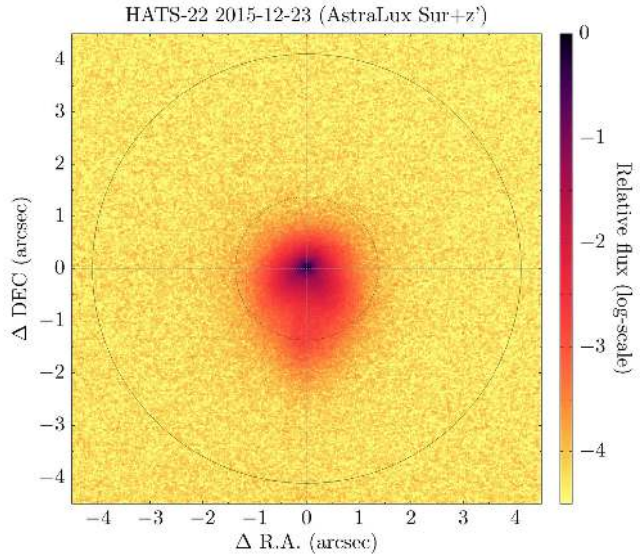

Figure 5. Lucky imaging observations of HATS-22 with the Astralux camera on the NTT telescope at La Silla in the z' band. We show the 1 and 4 arcsec radii lines for reference as well as the fitted centre of the star from the PSF modelling process. We note that the asymmetrical shape of the PSF is due to an instrumental effect related to non-stable focus on the telescope through the night. Similar patterns can be seen in other observations of this kind at similar times during the night.

The complete FGK-type star parameter space is searched using this method. We note that we do not treat micro- and macroturbulence as free parameters, but instead assume that these values are a function of atmospheric parameters and apply modifications to the synthetic spectra accordingly. To take into account the microturbulence dependence of the line widths, we computed an empirical relation between the microturbulence and the stellar parameters. In particular, we used the stellar parameters provided by the SweetCat (Santos et al. 2013) catalogue to define a polynomial that delivers the microturbulence as a function of $T_{\rm eff}$ and $\log g_*$. Then, the macroturbulence value used in the synthetization of each spectrum was obtained using that empirical function. More details on this method can be found in Brahm et al. (2017). This software used the combined spectra from the FEROS spectrograph taken for RV purposes. We calculate an initial estimate of the effective temperature ($T_{\rm eff}$), the surface gravity ($\log g$), metallicity ([Fe/H]) and projected stellar rotational velocity of the stars ($v \sin i$) and then use the Yonsei–Yale (YY; Yi et al. 2001) isochrones to obtain the remaining physical parameters. We do not, however, search for the best isochrone using the $\log g_*$ but instead use the stellar density ρ_*, which is well constrained by the photometric transit data and fitting routine. We then run the full set of parameters once again through a second iteration of ZASPE using the revised $\log g_*$ to improve the results. We present the adopted results and an extensive set of host star parameters from several sources in Table 6. We find HATS-22 to be a $V = 13.455 \pm 0.040$ magnitude solar metallicity K-type star with $T_{\rm eff} = 4803 \pm 55$ K and sub-solar mass and radius ($M_* = 0.759 \pm 0.019$ M$_\odot$ and $R_\star = 0.689^{+0.028}_{-0.018}$ R$_\odot$). HATS-23 ($V = 13.901 \pm 0.010$) and HATS-24 ($V = 12.830 \pm 0.010$) are determined to have super-solar masses and radii ($M_* = 1.115 \pm 0.054$ M$_\odot$; $R_* = 1.145 \pm 0.070$ R$_\odot$ and $M_* = 1.218 \pm 0.036$ M$_\odot$; $R_\star = 1.194^{+0.066}_{-0.041}$ R$_\odot$, respectively). HATS-23 is a G-type with a $T_{\rm eff}$ of 5780 ± 120 K and [Fe/H] of 0.280 ± 0.070 whilst HATS-24 is a solar metallicity F-type star with determined $T_{\rm eff} = 6346 \pm 81$ K.

Distances to these stars were determined by comparing the measured broad-band photometry listed in Table 6 to the predicted magnitudes in each filter from the isochrones. We assumed an $R_V = 3.1$ extinction law from Cardelli et al. (1989) to determine the extinction and find these to be consistent within their uncertainties to reddening maps available on the NASA/IPAC Infrared Science

Table 5. Orbital and planetary parameters for HATS-22b, HATS-23b and HATS-24b.

Parameter	HATS-22b Value	HATS-23b Value	HATS-24b Value
Light curve parameters			
P (d)	$4.722\,8124 \pm 0.000\,0052$	$2.160\,5156 \pm 0.000\,0045$	$1.348\,4954 \pm 0.000\,0013$
T_c (BJD)[a]	$2457078.58030 \pm 0.00022$	$2457072.85266 \pm 0.00070$	$2457038.47327 \pm 0.00038$
T_{14} (d)[a]	0.0913 ± 0.0015	0.0752 ± 0.0031	0.1008 ± 0.0010
$T_{12} = T_{34}$ (d)[a]	0.0154 ± 0.0014	0.094 ± 0.013	$0.012\,41 \pm 0.000\,81$
a/R_*	$15.70^{+0.39}_{-0.65}$	$6.08^{+0.41}_{-0.26}$	$4.67^{+0.10}_{-0.14}$
ζ/R_*[b]	$26.09^{+0.28}_{-0.19}$	56^{+28}_{-13}	22.64 ± 0.17
R_p/R_*	0.1426 ± 0.0025	0.159 ± 0.020	0.1307 ± 0.0030
b^2	$0.287^{+0.040}_{-0.064}$	$0.901^{+0.057}_{-0.090}$	$0.076^{+0.050}_{-0.045}$
b^2 lower limit[c]	–	>0.771	–
$b \equiv a\cos i/R_*$	$0.536^{+0.036}_{-0.064}$	$0.949^{+0.029}_{-0.049}$	$0.276^{+0.079}_{-0.101}$
b lower limit[c]	–	>0.878	–
i (deg)	87.96 ± 0.21	$81.02^{+0.93}_{-0.62}$	86.6 ± 1.2
i upper limit (deg)[c]	–	<83.5	–
HATSouth blend factors[d]			
Blend factor	0.861 ± 0.030	0.750 ± 0.062	0.787 ± 0.042
Limb-darkening coefficients[e]			
c_1, r	0.5808	0.3728	0.2638
c_2, r	0.1721	0.3215	0.3753
c_1, i	0.4355	0.2774	0.1919
c_2, i	0.2255	0.3334	0.3654
c_1, z	–	0.2116	–
c_2, z	–	0.3342	–
RV parameters			
K (m s^{-1})	399 ± 15	212.3 ± 8.6	396 ± 29
e[f]	0.079 ± 0.026	<0.114	<0.242
ω (deg)	56 ± 73	–	–
$\sqrt{e}\cos\omega$	$0.168^{+0.046}_{-0.062}$	–	–
$\sqrt{e}\sin\omega$	$0.225^{+0.084}_{-0.126}$	–	–
$e\cos\omega$	$0.043^{+0.016}_{-0.011}$	–	–
$e\sin\omega$	0.061 ± 0.040	–	–
RV jitter FEROS (m s^{-1})[g]	35 ± 28	0.0 ± 6.6	8 ± 52
RV jitter HARPS (m s^{-1})	1 ± 41	–	60 ± 140
RV jitter CORALIE (m s^{-1})	1 ± 41	–	70 ± 140
RV jitter CYCLOPS2+UCLES (m s^{-1})	–	–	72 ± 55
Planetary parameters			
M_p (M_J)	2.74 ± 0.11	1.470 ± 0.072	2.44 ± 0.18
R_p (R_J)	$0.953^{+0.048}_{-0.029}$	$1.86^{+0.30}_{-0.40}$	$1.487^{+0.078}_{-0.054}$
R_p lower limit (R_J)[c]	–	>1.31	–
$C(M_p, R_p)$[h]	0.20	0.23	−0.18
ρ_p (g cm^{-3})	3.89 ± 0.45	$0.29^{+0.30}_{-0.10}$	0.92 ± 0.15
$\log g_p$ (cgs)	3.868 ± 0.036	$3.02^{+0.21}_{-0.12}$	3.435 ± 0.054
a (au)	$0.050\,25 \pm 0.000\,42$	$0.033\,97 \pm 0.000\,47$	$0.025\,47 \pm 0.000\,23$
T_{eq} (K)	858^{+24}_{-17}	1654 ± 54	2067 ± 39
Θ[i]	0.378 ± 0.020	$0.0475^{+0.0131}_{-0.0067}$	$0.0684^{+0.0092}_{-0.0070}$
$\log_{10}\langle F\rangle$ (cgs)[j]	$8.088^{+0.048}_{-0.036}$	9.228 ± 0.058	9.615 ± 0.033

Notes. – For each system, we adopt the class of model that has the highest Bayesian evidence from among those tested. For HATS-23b and HATS-24b, the adopted parameters come from a fit in which the orbit is assumed to be circular. For HATS-22b, the eccentricity is allowed to vary.

[a]Times are in Barycentric Julian Date calculated directly from UTC *without* correction for leap seconds. T_c: reference epoch of mid-transit that minimizes the correlation with the orbital period. T_{14}: total transit duration, time between first to last contact; $T_{12} = T_{34}$: ingress/egress time, time between first and second, or third and fourth contact.

[b]Reciprocal of the half duration of the transit used as a jump parameter in our Markov chain Monte Carlo analysis in place of a/R_*. It is related to a/R_* by the expression $\zeta/R_\star = a/R_\star(2\pi(1 + e\sin\omega))/(P\sqrt{1-b^2}\sqrt{1-e^2})$ (Bakos et al. 2010).

[c]The grazing transits of HATS-23b mean that we cannot place a strong upper limit on the impact parameter. For this system, we also provide 95 per cent confidence lower limits on b^2, b and R_p, and the 95 per cent confidence upper limit on i.

[d]Scaling factor applied to the model transit that is fitted to the HATSouth light curves. This factor accounts for dilution of the transit due to blending from neighbouring stars and overfiltering of the light curve. These factors are varied in the fit.

[e]Values for a quadratic law, adopted from the tabulations by Claret (2004) according to the spectroscopic (ZASPE) parameters listed in Table 6.

[f]For fixed circular orbit models, we list the 95 per cent confidence upper limit on the eccentricity determined when $\sqrt{e}\cos\omega$ and $\sqrt{e}\sin\omega$ are allowed to vary in the fit.

[g]Term added in quadrature to the formal RV uncertainties for each instrument. This is treated as a free parameter in the fitting routine. In the cases where the jitter is consistent with zero, we list its 95 per cent confidence upper limit.

[h]Correlation coefficient between the planetary mass M_p and radius R_p estimated from the posterior parameter distribution.

[i]The Safronov number is given by $\Theta = \frac{1}{2}(V_{esc}/V_{orb})^2 = (a/R_p)(M_p/M_\star)$ (see Hansen & Barman 2007).

[j]Incoming flux per unit surface area, averaged over the orbit assuming a circular geometry.

Table 6. Stellar parameters for HATS-22, HATS-23 and HATS-24.

Parameter	HATS-22 Value	HATS-23 Value	HATS-24 Value	Source
Astrometric properties and cross-identifications				
2MASS-ID	2MASS 11360233-2932359	2MASS 19052800-5004024	2MASS 17553376-6144503	
GSC-ID	GSC 6664-00373	GSC 8382-01464	GSC 9054-00129	
RA (J2000)	$11^h36^m02^s.16$	$19^h05^m27^s.96$	$17^h55^m33^s.60$	2MASS
Dec. (J2000)	$-29°32'35''.9$	$-50°04'02''.5$	$-61°44'50''.3$	2MASS
μ_{RA} (mas yr^{-1})	27.1 ± 1.1	3.3 ± 1.4	2.9 ± 2.6	UCAC4
$\mu_{Dec.}$ (mas yr^{-1})	-8.7 ± 1.4	-1.1 ± 1.5	-11.0 ± 2.6	UCAC4
Spectroscopic properties				
$T_{eff\star}$ (K)	4803 ± 55	5780 ± 120	6346 ± 81	ZASPE[a]
[Fe/H] (dex)	0.000 ± 0.040	0.280 ± 0.070	0.000 ± 0.050	ZASPE
$v \sin i$ (km s^{-1})	0.50 ± 0.50	4.62 ± 0.49	9.44 ± 0.21	ZASPE
v_{mac} (km s^{-1})	2.49	4.00	4.87	Assumed
v_{mic} (km s^{-1})	0.58	1.08	1.56	Assumed
γ_{RV} (m s^{-1})	-7370 ± 23	$-13\,372.0 \pm 6.1$	-3259 ± 41	CORALIE or FEROS[b]
Photometric properties				
B (mag)	14.496 ± 0.040	14.625 ± 0.010	13.404 ± 0.010	APASS[c]
V (mag)	13.455 ± 0.040	13.901 ± 0.010	12.830 ± 0.010	APASS[c]
g (mag)	13.943 ± 0.030	14.246 ± 0.010	13.071 ± 0.010	APASS[c]
r (mag)	13.056 ± 0.030	13.735 ± 0.010	12.643 ± 0.010	APASS[c]
i (mag)	12.82 ± 0.14	13.427 ± 0.010	12.518 ± 0.090	APASS[c]
J (mag)	11.556 ± 0.023	12.636 ± 0.025	11.678 ± 0.022	2MASS
H (mag)	11.006 ± 0.022	12.293 ± 0.025	11.447 ± 0.025	2MASS
K_s (mag)	10.942 ± 0.019	12.262 ± 0.030	11.382 ± 0.023	2MASS
Derived properties				
M_* ($M_\odot$)	0.759 ± 0.019	1.121 ± 0.046	1.212 ± 0.033	YY+ρ_*+ZASPE[d]
R_* ($R_\odot$)	$0.689^{+0.028}_{-0.018}$	$1.199^{+0.061}_{-0.081}$	1.172 ± 0.033	YY+ρ_*+ZASPE
$\log g_*$ (cgs)	4.644 ± 0.028	4.328 ± 0.044	4.384 ± 0.021	YY+ρ_*+ZASPE
ρ_* (g cm^{-3})[e]	3.26 ± 0.68	$0.92^{+0.20}_{-0.11}$	$1.096^{+0.059}_{-0.085}$	Light curves
ρ_* (g cm^{-3})[e]	$3.28^{+0.25}_{-0.39}$	$0.91^{+0.20}_{-0.11}$	1.059 ± 0.075	YY+Light curves+ZASPE
L_* ($L_\odot$)	$0.226^{+0.026}_{-0.020}$	1.43 ± 0.22	1.96 ± 0.18	YY+ρ_*+ZASPE
M_V (mag)	6.71 ± 0.13	4.43 ± 0.18	4.03 ± 0.10	YY+ρ_*+ZASPE
M_K (mag, ESO)	4.359 ± 0.081	2.90 ± 0.13	2.844 ± 0.065	YY+ρ_*+ZASPE
Age (Gyr)	–[f]	4.2 ± 1.5	$0.88^{+0.67}_{-0.45}$	YY+ρ_*+ZASPE
A_V (mag)	0.151 ± 0.084	0.106 ± 0.075	0.261 ± 0.061	YY+ρ_*+ZASPE
Distance (pc)	$207.9^{+8.9}_{-6.6}$	747 ± 46	510 ± 15	YY+ρ_*+ZASPE

Notes. – For each system, we adopt the class of model that has the highest Bayesian evidence from among those tested. For HATS-23 and HATS-24, the adopted parameters come from a fit in which the orbit is assumed to be circular. For HATS-22, the eccentricity is allowed to vary.

[a] ZASPE = Zonal Atmospherical Stellar Parameter Estimator routine for the analysis of high-resolution spectra (Brahm et al. 2017), applied to the FEROS spectra of HATS-22, HATS-23 and HATS-24. These parameters rely primarily on ZASPE, but have a small dependence also on the iterative analysis incorporating the isochrone search and global modelling of the data.

[b] This is based on CORALIE for HATS-22 and FEROS for HATS-23 and HATS-24. The error on γ_{RV} is determined from the orbital fit to the RV measurements, and does not include the systematic uncertainty in transforming the velocities to the IAU standard system. The velocities have not been corrected for gravitational redshifts.

[c] From APASS DR6 (Henden et al. 2009) for as listed in the UCAC 4 catalogue (Ochsenbein, Bauer & Marcout 2000).

[d] YY+ρ_*+ZASPE = Based on the YY isochrones (Yi et al. 2001), ρ_* as a luminosity indicator, and the ZASPE results.

[e] In the case of ρ_*, we list two values. The first value is determined from the global fit to the light curves and RV data, without imposing a constraint that the parameters match the stellar evolution models. The second value results from restricting the posterior distribution to combinations of ρ_*+$T_{eff\star}$+[Fe/H] that match to a YY stellar model.

[f] Omitted due to large uncertainty. Isochrone models (cf. Fig. 6) are unable to constrain age for this system.

Archive.[1] The locations of each star on a $T_{eff\star}$–ρ_* diagram (similar to a Hertzsprung–Russell diagram) are shown in Fig. 6.

[1] Publicly available at http://irsa.ipac.caltech.edu/applications/DUST/.

3.2 Excluding blend scenarios

In order to exclude blend scenarios, we carried out an analysis following Hartman et al. (2012). We model the available photometric data (including light curves and catalogue broad-band photometric measurements) for each object as a blend between an eclipsing binary star system and a third star along the line of sight. The physical properties of the stars are constrained using the Padova isochrones

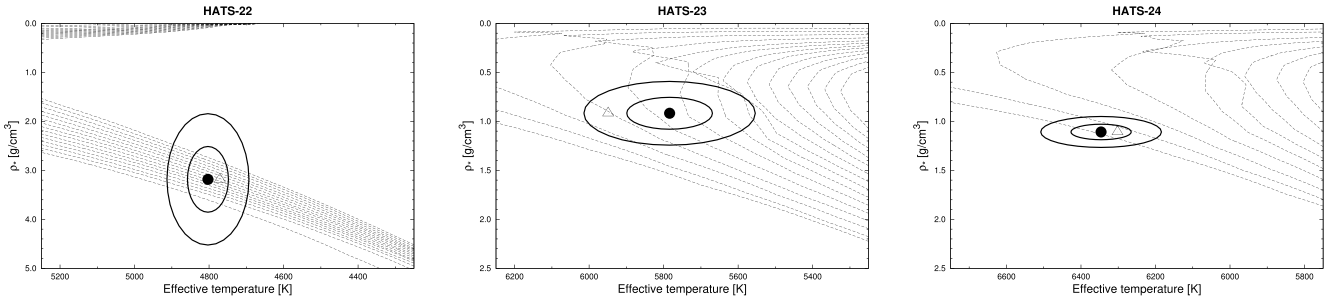

Figure 6. Model isochrones from Yi et al. (2001) for the measured metallicities of HATS-22 (left), HATS-23 (middle) and HATS-24 (right). We show models for ages of 0.2 Gyr and 1.0–14.0 Gyr in 1.0 Gyr increments (ages increasing from left to right). The adopted values of $T_{\rm eff\star}$ and ρ_* are shown together with their 1σ and 2σ confidence ellipsoids. The initial values of $T_{\rm eff\star}$ and ρ_* from the first ZASPE and light-curve analyses are represented with a triangle.

(Girardi et al. 2000), while we also require that the brightest of the three stars in the blend have atmospheric parameters consistent with those measured with ZASPE. We also simulate composite cross-correlation functions and use them to predict RVs and BSs for each blend scenario considered. For HATS-22, all blend scenarios tested can be rejected with greater than 3σ confidence, based on the photometry alone. Those models that cannot be rejected with at least 5σ confidence would have obviously double-lined spectra, and would also have BS variations in excess of 1 km s^{-1}. For HATS-23, all blend scenarios tested can be rejected with greater than 3.3σ confidence based on the photometry. Although some of the models that cannot be rejected with at least 5σ confidence do predict low-amplitude BS and RV variations, the simulated RVs do not reproduce the sinusoidal variation with the orbital period that is clearly detected (Fig. 3). For HATS-24, all blend scenarios tested can be rejected with greater than 4σ confidence based on the photometry. Those that cannot be rejected with at least 5σ confidence yield large-amplitude RV and BS variations in excess of 1 km s^{-1}. We conclude that all three objects are transiting planet systems; however, we cannot exclude the possibility that one or more of these objects are an unresolved binary stellar system with one component hosting a short-period transiting planet (see Section 2.4). For the remainder of the paper, we assume that these are all single stars with transiting planets, but we note that the radii, and potentially the masses, of the planets would be larger than what we infer here if subsequent observations reveal binary star companions.

3.3 Global modelling of the data

We modelled the HATSouth photometry, the follow-up photometry and the high-precision RV measurements following Pál et al. (2008), Bakos et al. (2010) and Hartman et al. (2012). We fit Mandel & Agol (2002) transit models to the light curves, allowing for a dilution of the HATSouth transit depth as a result of blending from neighbouring stars and overcorrection by the trend-filtering method. To correct for systematic errors in the follow-up light curves, we include in our model, for each event, a quadratic trend in time. Linear trends with up to three parameters describing the position and shape of the PSF are also included to compensate for any systematic effects due to poor guiding or PSF shape changes throughout the transit observation. We fit Keplerian orbits to the RV curves allowing the zero-point for each instrument to vary independently in the fit, and allowing for RV jitter that we also vary as a free parameter for each instrument. We used a Differential Evolution Markov chain Monte Carlo procedure to explore the fitness landscape and to determine the posterior distribution of the parameters.

We tried to both fit fixed circular orbit models and models with the eccentricity as a free parameter and then used the method of Weinberg, Yoon & Katz (2013) to estimate the Bayesian evidence for each scenario. We find a higher evidence for a non-circular orbital solution (by a factor of 80) for HATS-22b and find the most likely eccentricity to be $e = 0.079 \pm 0.026$. For HATS-23b and HATS-24b, the fixed circular orbit models have the higher evidence; for HATS-23, the circular model has an evidence that is 20 times greater than the free-eccentricity model, while for HATS-24b the circular model has an evidence that is 70 times greater. We therefore adopt the parameters from the circular orbit models for these two systems, placing 95 per cent confidence upper limits on their eccentricity as $e < 0.114$ and $e < 0.242$, respectively. The results of the fitting routines for each planet can be found in Table 5.

The grazing nature of HATS-23b naturally leads to a higher uncertainty on the determination of specific parameters typically constrained by the depth and shape of the transit. As a consequence of this, in Table 5 we have indicated the best-fitting results (with the corresponding 1σ confidence) as well as lower limits for selected parameters. In particular, the poor constraint on the impact parameter from the photometric follow-up light curves should be noted. This in turn affects the estimates of the orbital inclination, the planet radius and orbital separation. We also note that the larger uncertainties in the bottom light curvefor this planet are due to the fact that the data were taken in the z band. Whilst inclusion of these data in the transit fitting process has a minimal impact on the parameter estimation, the blend scenario analysis process (cf. Section 3.2) benefited from this data set. The consistency between this partial transit and those observed in the i band limits the range of blend models that can fit the observations. Nevertheless, significantly higher precision multi-band follow-up would be required to improve the characterization of this system.

4 DISCUSSION

In this work, we report the discovery of three new moderately high-mass hot Jupiters by the HATSouth survey: HATS-22b, HATS-23b and HATS-24b. These planets add to the growing numbers of known hot Jupiters and provide vital additional insights into the formation and distribution of short-period massive planets. In Figs 7 and 8, we show these discoveries in the context of known planets with masses higher than $0.5M_{\rm J}$ and less than 10 d orbital periods.[2]

[2] Previously known planets taken from the NASA Exoplanet Archive at http://exoplanetarchive.ipac.caltech.edu/ on 02/02/2017.

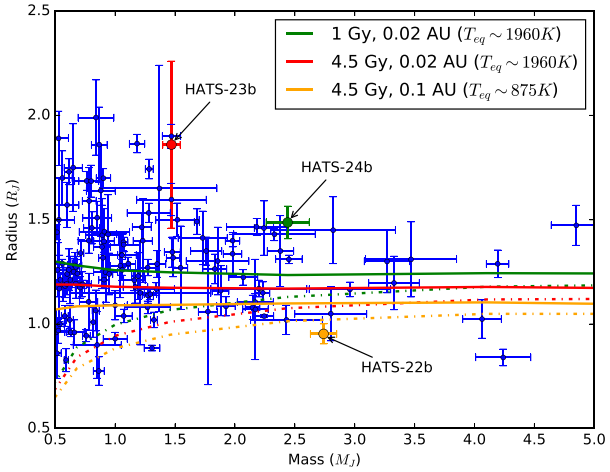

Figure 7. Mass–radius relation for hot Jupiters, defined as those planets with masses higher than $0.5M_J$ and periods shorter than 10 d. We show theoretical models for planet structures from Fortney, Marley & Barnes (2007) for each of the three planets announced in this paper for both no core (solid lines) and 100 $M_\oplus$ core (dashed lines) scenarios. The new HATSouth planets are indicated. 4.5 Gyr, 0.1 au models are shown for comparison with HATS-22b (yellow lines). The 4.5 Gyr, 0.02 au models (red lines) are used as equivalent examples for HATS-23b and the models for HATS-24b (1 Gyr, 0.02 au) are shown in green lines.

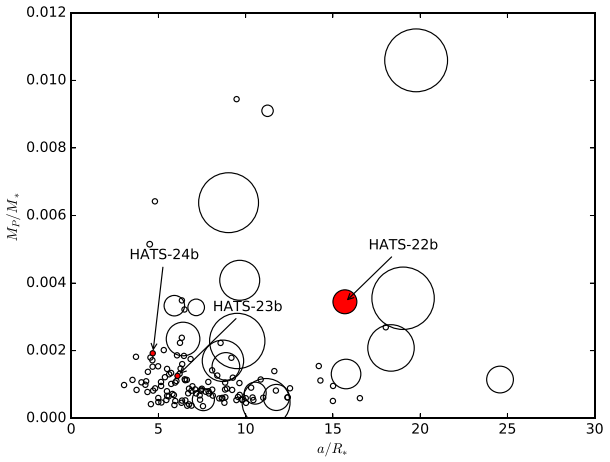

Figure 8. Planet-to-star mass ratio as a function of the ratio between the orbital separation and the stellar radius for known hot Jupiters. We have labelled our new discoveries in the plot, which are marked as filled red symbols. The dot sizes correspond to the planets' measured eccentricity ranging from zero (smallest size) up to a value of 0.562.

4.1 Mass–radius relation

In Fig. 7, we plot a mass–radius relation for known hot Jupiters, highlighting our three new discovered planets. Additionally, this plot contains a selection of predicted mass–radius relations from Fortney et al. (2007) that are closest to the conditions of each of these planets. For HATS-23b and HATS-24b (red and green curves, respectively), we have selected those models that most closely matched the determined age and orbital separation of the planets (4.5 and 1 Gyr, respectively, at 0.02 au separation) and with orbital periods of less than 10 d. These models assume a solar analogue host star and solar luminosity. For HATS-22b, however, due to the lower luminosity of the host star, we have selected the curve that most closely matches the expected equilibrium temperature $T_{\rm eq}$ for this planet, a 4.5 Gyr model at 0.1 au, which is equivalent to a $T_{\rm eq}$ of approximately 875 K, thereby matching the model to the planet's conditions. In all cases, we plot the two extreme limits of planetary core mass: no core (solid line) and a 100 $M_\oplus$ core model (dashed line). Despite the fact that none of the target's radii fall within their equivalent predicted mass–radius range from the model curves, HATS-22b is consistent with a high-mass (100 $M_\oplus$) core at a 95 per cent confidence level. This places this planet among the 20 highest bulk density hot Jupiters known to date, defined as those with masses higher than $0.5M_J$ and less than 10 d orbital periods. While we are not able to confidently make any conclusions regarding the structure of grazing transiting planet HATS-23b, we note that even assuming the lower limit on the radius of this planet at $1.31M_J$, it is still more likely that this is an example of a low core mass hot Jupiter.

Perhaps the most interesting case in this context is that of HATS-24b. The radius of this planet is estimated more than 3σ above the model line for a pure helium–hydrogen planet at approximately this age and orbital separation. The short period and young age of the host star lead to a high equilibrium temperature ($T_{\rm eq} = 2067 \pm 39$ K), which puts it in a similar regime to other inflated hot Jupiters (e.g. WASP-71b, Smith et al. 2013 and HATS-35b, de Val-Borro et al. 2016). As noted by Marley et al. (2007) and Fortney et al. (2007), the physical properties of giant planets at young ages are uncertain, and the model shown does not include considerations on the formation mechanism. The somewhat inflated radius of this planet may be due to a combination of mechanisms discussed in Section 1. Additionally, the apparent higher radius may be due to an ongoing evaporation of the upper layers of the planet's atmosphere as current models are unable to explain the radius of HATS-24b. This factor, coupled with the fact that the host star is moderately bright ($V = 12.830 \pm 0.010$) and the large transit depth signal, makes this a good target for further wavelength-dependent transmission studies with large-class telescopes. Assuming a hydrogen-dominated atmosphere, the scaleheight H for this planet is estimated at 314.8 ± 32.8 km, a value comparable to other inflated hot Jupiters. Therefore, a transmission spectroscopic signal equivalent to 5 scaleheights would be detectable at a level of $\sim$250 ppm, well within the capability of current and future facilities.

4.2 Eccentricity and tidal circularization

A comparative study between the three announced planets and previously known hot Jupiters is useful as the orbital eccentricity is an important parameter thought to be highly related to planetary migration both in disc interaction and planet scattering scenarios. As discussed in Section 1, eccentric orbits are found preferentially for higher mass planets (e.g. Southworth et al. 2009) and a higher orbital separation seems to correspond with non-zero eccentricity (Pont et al. 2011). This supports the fact that a high-mass planet at a large separation should require more time for tidal circularization.

Our analysis (discussed in Section 3.3) finds HATS-22b to be the only planet of the three with a likely non-zero eccentricity of $e = 0.079 \pm 0.026$. The distinction between HATS-22b and the two other planets discovered in this work is made more evident in Fig. 8, in which we have plotted the planet-to-stellar mass ratio as a function of the ratio between the orbital separation and the stellar radius ($a/R_\star$). These parameters are the dominant factors in determining the tidal circularization time-scale of planetary orbits (Ogilvie 2014; Duffell & Chiang 2015) in which the mass ratio is

proportional to the circularization time-scale. This is due to the fact that more massive planets are more likely to carve a large gap in the protoplanetary disc, leading to less efficient circularization due to disc interaction. Thus, these planets should remain in moderate non-zero eccentric orbits for a longer time. In Fig. 8, the dot sizes correspond to the eccentricity values, ranging from zero to 0.562, where the concentration of low- or zero-eccentricity planets can be found for low values of both plotted parameters. HATS-22b can be seen occupying a region of parameter space clearly distinguished from that of HATS-23b and HATS-24b, suggesting that the eccentric orbit of HATS-22b may indeed be a result of insufficient time for full tidal circularization. However, several examples can still be found in this figure that are inconsistent with this picture. The case of CoRoT-27b (Parviainen et al. 2014) is of a non-eccentric orbit planet that can be seen as the point with a mass ratio just under 0.01. Despite the moderate age of this system (4.21 ± 2.72 Gyr), a planet with such a high mass ratio is still predicted to be found in an eccentric orbit. On the other hand, several cases can also be found with low values of both parameters plotted in Fig. 8 that still presently show detectable orbital eccentricity, suggesting that there are other mechanisms, besides tidal circularization, determining the eccentricity distribution of exoplanets.

ACKNOWLEDGEMENTS

The HATSouth network is operated by a collaboration consisting of Princeton University (PU), the Max Planck Institute für Astronomie (MPIA), the Australian National University (ANU) and the Pontificia Universidad Católica de Chile (PUC). The station at Las Campanas Observatory (LCO) of the Carnegie Institute is operated by PU in conjunction with PUC, the station at the High Energy Spectroscopic Survey (H.E.S.S.) site is operated in conjunction with MPIA, and the station at Siding Spring Observatory (SSO) is operated jointly with ANU. Based in part on data collected at Subaru Telescope, which is operated by the National Astronomical Observatory of Japan. Also based in part on observations made with the MPG 2.2 m telescope at the ESO Observatory in La Silla. Development of the HATSouth project was funded by NSF MRI grant NSF/AST-0723074, operations have been supported by NASA grants NNX09AB29G and NNX12AH91H, and follow-up observations receive partial support from grant NSF/AST-1108686. AJ acknowledges support from FONDECYT project 1130857, BASAL CATA PFB-06 and project IC120009 'Millennium Institute of Astrophysics (MAS)' of the Millennium Science Initiative, Chilean Ministry of Economy. RB and NE are supported by CONICYT-PCHA/Doctorado Nacional. They also acknowledge additional support from project IC120009 'Millennium Institute of Astrophysics (MAS)' of the Millennium Science Initiative, Chilean Ministry of Economy. VS acknowledges support form BASAL CATA PFB-06. MR acknowledges support from FONDECYT postdoctoral fellowship 3120097. This work is based on observations made with ESO Telescopes at the La Silla Observatory. This paper also uses observations obtained with facilities of the Las Cumbres Observatory Global Telescope. Work at the Australian National University is supported by ARC Laureate Fellowship Grant FL0992131. We acknowledge the use of the AAVSO Photometric All-Sky Survey (APASS), funded by the Robert Martin Ayers Sciences Fund, and the SIMBAD data base, operated at CDS, Strasbourg, France. Operations at the MPG 2.2 m telescope are jointly performed by the Max Planck Gesellschaft and the European Southern Observatory. The imaging system GROND has been built by the high-energy group of MPE in collaboration with the LSW Tautenburg and ESO. We thank Régis Lachaume for his technical assistance during the observations at the MPG 2.2 m telescope. We also thank Helmut Steinle and Jochen Greiner for supporting the GROND observations presented in this manuscript. We are grateful to P. Sackett for her help in the early phase of the HATSouth project. This research has made use of the NASA/IPAC Infrared Science Archive, which is operated by the Jet Propulsion Laboratory, California Institute of Technology, under contract with the National Aeronautics and Space Administration. Observing times were obtained through proposals CN2013A-171, CN2013B-55, CN2014A-104, CN2014B-57, CN2015A-51 and ESO 096.C-0544. This research has made use of the NASA Exoplanet Archive, which is operated by the California Institute of Technology, under contract with the National Aeronautics and Space Administration under the Exoplanet Exploration Program.

REFERENCES

Addison B. C., Tinney C. G., Wright D. J., Bayliss D., Zhou G., Hartman J. D., Bakos G. Á., Schmidt B., 2013, ApJ, 774, L9
Alibert Y., Mordasini C., Benz W., Winisdoerffer C., 2005, A&A, 434, 343
Antonini F., Hamers A. S., Lithwick Y., 2016, AJ, 152, 174
Bakos G. Á. et al., 2010, ApJ, 710, 1724
Bakos G. Á. et al., 2013, PASP, 125, 154
Batygin K., Bodenheimer P. H., Laughlin G. P., 2016, ApJ, 829, 114
Bayliss D. et al., 2013, AJ, 146, 113
Bayliss D. et al., 2015, AJ, 150, 49
Bento J. et al., 2014, MNRAS, 437, 1511
Bodenheimer P., Hubickyj O., Lissauer J. J., 2000, Icarus, 143, 2
Boss A. P., 1995, Science, 267, 360
Brahm R., Jordan A., Hartman J., Bakos G., 2017, MNRAS, 467, 971
Brahm R. et al., 2016, AJ, 151, 89
Brown T. M. et al., 2013, PASP, 125, 1031
Cardelli J. A., Clayton G. C., Mathis J. S., 1989, ApJ, 345, 245
Chambers J. E., 2009, ApJ, 705, 1206
Claret A., 2004, A&A, 428, 1001
Collier Cameron A., Bruce V. A., Miller G. R. M., Triaud A. H. M. J., Queloz D., 2010, MNRAS, 403, 151
Croll B., Lafreniere D., Albert L., Jayawardhana R., Fortney J. J., Murray N., 2011, AJ, 141, 30
de Val-Borro M. et al., 2016, AJ, 152, 161
Désert J.-M. et al., 2011, ApJS, 197, 11
Donati J. F. et al., 2016, Nature, 534, 662
Dopita M., Hart J., McGregor P., Oates P., Bloxham G., Jones D., 2007, Ap&SS, 310, 255
Duffell P. C., Chiang E., 2015, ApJ, 812, 94
Ford E. B., Rasio F. A., 2008, ApJ, 686, 621
Fortney J. J., Marley M. S., Barnes J. W., 2007, ApJ, 659, 1661
Fruchter A. S., Hook R. N., 2002, PASP, 114, 144
Gandolfi D. et al., 2012, A&A, 543, L5
Girardi L., Bressan A., Bertelli G., Chiosi C., 2000, A&AS, 141, 371
Gustafsson B., Edvardsson B., Eriksson K., Jørgensen U. G., Nordlund Å., Plez B., 2008, A&A, 486, 951
Hansen B. M. S., Barman T., 2007, ApJ, 671, 861
Hartman J. D. et al., 2012, AJ, 144, 139
Hartman J. D. et al., 2015, AJ, 150, 197
Henden A. A., Welch D. L., Terrell D., Levine S. E., 2009, BAAS, 41, 669
Hippler S. et al., 2009, The Messenger, 137, 14
Jordán A. et al., 2013, ApJ, 778, 184
Jordán A. et al., 2014, AJ, 148, 29
Kaufer A., Pasquini L., 1998, in D'Odorico S., ed., Proc. SPIE, Vol. 3355, Optical Astronomical Instrumentation. SPIE, Bellingham, p. 844
Knutson H. A., Charbonneau D., Allen L. E., Burrows A., Megeath S. T., 2008, ApJ, 673, 526
Kovács G., Zucker S., Mazeh T., 2002, A&A, 391, 369
Kovács G., Bakos G., Noyes R. W., 2005, MNRAS, 356, 557

Kozai Y., 1962, AJ, 67, 591
Lissauer J. J., 1995, Icarus, 114, 217
Lithwick Y., Wu Y., 2011, ApJ, 739, 31
Louden T., Wheatley P. J., 2015, ApJ, 814, L24
Mandel K., Agol E., 2002, ApJ, 580, L171
Marcy G. W., Butler R. P., Vogt S. S., Fischer D. A., Henry G. W., Laughlin G., Wright J. T., Johnson J. A., 2005, ApJ, 619, 570
Marley M. S., Fortney J. J., Hubickyj O., Bodenheimer P., Lissauer J. J., 2007, ApJ, 655, 541
Marley M. S., Ackerman A. S., Cuzzi J. N., Kitzmann D., 2013, in Mackwell S. J., Simon-Miller A. A., Harder J. W., Bullock M. A., eds, Comparative Climatology of Terrestrial Planets. Univ. Arizona Press, Tucson, p. 367
Mayor M. et al., 2003, The Messenger, 114, 20
Mazeh T., Mayor M., Latham D. W., 1997, ApJ, 478, 367
Ngo H. et al., 2016, ApJ, 827, 8
Ochsenbein F., Bauer P., Marcout J., 2000, A&AS, 143, 23
Ogilvie G. I., 2014, ARA&A, 52, 171
Pál A. et al., 2008, ApJ, 680, 1450
Parviainen H. et al., 2014, A&A, 562, A140
Penev K. et al., 2013, AJ, 145, 5
Petrovich C., 2015, ApJ, 805, 75
Pont F., Knutson H., Gilliland R. L., Moutou C., Charbonneau D., 2008, MNRAS, 385, 109
Pont F., Husnoo N., Mazeh T., Fabrycky D., 2011, MNRAS, 414, 1278
Queloz D. et al., 2001, The Messenger, 105, 1
Rasio F. A., Ford E. B., 1996, Science, 274, 954
Rice W. K. M., Armitage P. J., Hogg D. F., 2008, MNRAS, 384, 1242
Santos N. C. et al., 2013, A&A, 556, A150
Schlaufman K. C., Winn J. N., 2016, ApJ, 825, 62
Seager S., Sasselov D. D., 2000, ApJ, 537, 916
Sing D. K. et al., 2011, MNRAS, 416, 1443
Smith A. M. S. et al., 2013, A&A, 552, A120
Southworth J. et al., 2009, ApJ, 707, 167
Struve O., 1952, The Observatory, 72, 199
Weinberg M. D., Yoon I., Katz N., 2013, Bayesian Analysis, preprint (arXiv:1301.3156)
Wu Y., Lithwick Y., 2011, ApJ, 735, 109
Wu Y., Murray N., 2003, ApJ, 589, 605
Yi S., Demarque P., Kim Y.-C., Lee Y.-W., Ree C. H., Lejeune T., Barnes S., 2001, ApJS, 136, 417
Zechmeister M., Kürster M., 2009, A&A, 496, 577
Zhou G., Kedziora-Chudczer L., Bayliss D. D. R., Bailey J., 2013, ApJ, 774, 118
Zhou G., Bayliss D. D. R., Kedziora-Chudczer L., Salter G., Tinney C. G., Bailey J., 2014, MNRAS, 445, 2746
Zhou G., Latham D. W., Bieryla A., Beatty T. G., Buchhave L. A., Esquerdo G. A., Berlind P., Calkins M. L., 2016, MNRAS, 460, 3376

This paper has been typeset from a TEX/LATEX file prepared by the author.